PHOTONICS Research

Intermodal frequency generation in silicon-rich silicon nitride waveguides

C. Lacava,[1,*] T. Dominguez Bucio,[1] A. Z. Khokhar,[1] P. Horak,[1] Y. Jung,[1] F. Y. Gardes,[1] D. J. Richardson,[1] P. Petropoulos,[1] and F. Parmigiani[1,2]

[1]Optoelectronics Research Centre, University of Southampton, SO17 1BJ, Southampton, UK
[2]Currently at Microsoft Research UK, CB1 2FB, Cambridge, UK
*Corresponding author: C.Lacava@soton.ac.uk

Received 1 February 2019; revised 26 March 2019; accepted 26 March 2019; posted 27 March 2019 (Doc. ID 359361); published 3 May 2019

Dispersion engineering in optical waveguides allows applications relying on the precise control of phase matching conditions to be implemented. Although extremely effective over relatively narrow band spectral regions, dispersion control becomes increasingly challenging as the bandwidth of the process of interest increases. Phase matching can also be achieved by exploiting the propagation characteristics of waves exciting different spatial modes of the same waveguide. Phase matching control in this case relies on achieving very similar propagation characteristics across two, and even more, waveguide modes over the wavelengths of interest, which may be rather far from one another. We demonstrate here that broadband (>40 nm) four-wave mixing can be achieved between pump waves and a signal located in different bands of the communications spectrum (separated by 50 nm) by exploiting interband nonlinearities. Our demonstration is carried out in the silicon-rich silicon nitride material platform, which allows flexible device engineering, allowing for strong effective nonlinearity at telecommunications wavelengths without deleterious nonlinear-loss effects.

https://doi.org/10.1364/PRJ.7.000615

1. INTRODUCTION

The insatiable demand for communication traffic necessitates the adoption of radically new approaches in the implementation of optical transmission systems. One particularly attractive route to increase the data carrying capacity of optical fiber communication systems stems from the observation that current systems utilize only a very small portion of the low-loss bandwidth of silica optical fibers. Therefore, solutions that exploit wavelengths outside the conventional C-band spectrum (1530–1565 nm) are actively being explored, and the first long-haul transmission systems utilizing the adjacent L-band (1565–1625 nm) have recently been deployed. In these new systems, the ability to generate and manipulate wavelength components that are placed at extremely distant positions in the spectrum with respect to a common source placed in the C-band is highly desirable. Third-order nonlinear devices offer the possibility to generate new wavelength components through parametric processes such as those based on four-wave mixing (FWM) [1]. Considerable efforts have been devoted to the realization of wavelength converters and synthesizers, based either on optical fibers [1] or integrated waveguides [2,3], that are capable of operating over a broad wavelength span. In general, these devices have exploited nonlinear processes arising within a single spatial mode. However, recent works have shown the potential offered by the use of intermodal (IM) nonlinearities, namely, the nonlinear interaction between waves copropagating within different spatial modes of the same optical waveguide [4–7]. By engineering the characteristics of distinct spatial modes over the wavelengths of interest, IM-FWM allows the interaction between wavelengths that may in principle be spaced, as widely even as 500 nm from one another [8]. Recently, various demonstrations of IM-based applications have been shown, such as the generation of the supercontinuum [9–11], the realization of fiber lasers [12,13], beam-forming applications [14], and frequency conversion [4–6,12,15–21]. However, even though promising results have been demonstrated to date, reported implementations of IM-FWM have been shown to take place within a rather localized bandwidth (<10 nm) around the phase-matched wavelengths, mainly restricted by fabrication imperfections and the limited design capabilities offered by the material platforms so far employed. In the work we report in this paper, we achieve a step change improvement over previous reported results, facilitated through the adoption of the silicon-rich silicon nitride platform [22], which allows fine tuning of the waveguide refractive index profile, and, therefore, excellent dispersion engineering control.

Moreover, unlike silicon itself, the material can be engineered to show strong Kerr nonlinearities without the onset of two-photon absorption (TPA) at telecommunication wavelengths, enabling the development of high-efficiency devices with low losses. In our experiments, IM-FWM is based on a dual-pump Bragg scattering (BS) scheme implemented over two spatial modes. Wavelength conversion over a bandwidth exceeding 40 nm in the L-band was performed using two pump waves placed in the C-band. We measured a conversion efficiency (calculated as the ratio between the output idler and the output signal power levels) of −15 dB for a total pump power of 32 dBm at the input of the waveguide. We note that a relatively high pump power level was required to achieve such a level of conversion efficiency. Further material developments are needed to reduce the waveguide losses. This would enable use of longer waveguide sections, thus allowing use of lower pump power levels and possibly achieving higher conversion efficiency values.

2. DUAL-PUMP BRAGG SCATTERING IM-FWM SCHEME

Among the various types of FWM, BS enables the generation of frequencies (blue- and red-shifted replicas of the original signal), in principle in a noiseless manner [23]. Referring to Fig. 1 (top panel), the idler frequencies of $I_{\mathrm{BS},r}$ or $I_{\mathrm{BS},b}$, respectively, are determined by the energy conservation law; i.e., they appear at $\omega_s \pm \Delta\omega$, where ω_s is the signal frequency and $\Delta\omega$ is the pump-to-pump wavelength detuning. The arrows indicate gain (up) and loss (down) of the photon energy. As in any FWM-based process, efficient conversion is guaranteed only when phase matching among the interacting waves is satisfied. In single-mode waveguides, this is typically achieved by tailoring the waveguide geometry to engineer the group velocity dispersion [24]. Efficient BS FWM then requires the waveguide to exhibit zero dispersion at the half-distance between the average frequency of the pair of pumps and that of the signal–idler pair [23]. The phase matching conditions in the IM case, however, give rise to distinctly different conditions.

In our experiments, the two pumps, P_1 and P_2, were placed into the fundamental TE00 mode, while the signal and the generated idlers were in the first-order TE10 mode. A schematic of the phase matching process of IM-FWM for the $I_{\mathrm{BS},r}$ or $I_{\mathrm{BS},b}$, respectively, is illustrated in Fig. 1 (bottom panel) [4,6,16,25], where the inverse group velocity (v_g^{-1}) curves of the modes supported in a multimode waveguide are shown as a function of frequency. Phase matching for the $I_{\mathrm{BS},r}$ idler is satisfied when the following equation is fulfilled:

$$-\beta^0(\omega_{P1}) + \beta^1(\omega_S) + \beta^0(\omega_{P2}) - \beta^1(\omega_{\mathrm{BS},r}) = 0, \tag{1}$$

where $\beta^0(\omega)$ and $\beta^1(\omega)$ indicate the propagation constants of two generic modes, 0 and 1, at frequency ω, respectively, and ω_i is the frequency of pump 1, pump 2, signal, and redshifted BS idler for $i = P1$, $P2$, S, and BSr, respectively. Equation (1) can be conveniently rewritten as

$$\beta^0(\omega_{P1}) - \beta^0(\omega_{P2}) = \beta^1(\omega_S) - \beta^1(\omega_{\mathrm{BS},r}), \tag{2}$$

$$\beta^0(\omega_{P1}) - \beta^0(\omega_{P1} - \Delta\omega) = \beta^1(\omega_S) - \beta^1(\omega_S - \Delta\omega). \tag{3}$$

For a small frequency detuning ($\Delta\omega \approx 0$), Eq. (3) indicates that phase matching is achieved when the derivative function of the propagation constant in one mode, calculated at ω_{P1}, that is its inverse group velocity, is the same as that in the other mode,

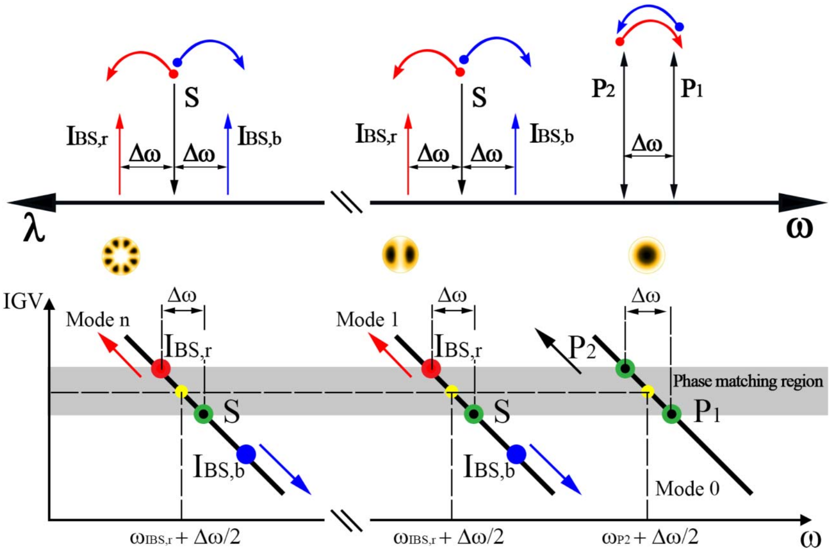

Fig. 1. (Top panel) Dual-pump Bragg scattering operation principle. When two pumps (P_1 and P_2) and a signal (S) are injected in third-order nonlinear media, Bragg scattering can occur if the phase matching condition is satisfied. Photons are scattered from the signal (S) to two idlers ($I_{\mathrm{BS},r}$ and $I_{\mathrm{BS},b}$), and energy exchange also occurs between the two pumps (P_1 and P_2). This mechanism can be employed to realize wavelength conversion and wavelength exchange functionalities. (Bottom panel) Graph illustrating the phase matching mechanism between spatial modes in a multimode waveguide. If the two pumps (P_1 and P_2) are placed in the first-order mode (mode 0) and the signal and idlers in the second-order mode (mode 1), the phase matching condition can be realized and retained if a horizontal line that crosses the inverse group velocity (IGV) curves of the two considered modes can be drawn, intercepting the average frequencies of the two pumps and the signal and one idler [either $I_{\mathrm{BS},r}$ or $I_{\mathrm{BS},b}$ (yellow dots in the figure)].

calculated at ω_S [6]. This means that the crossing of any horizontal line drawn on the group velocity curves of Fig. 1 (bottom panel) indicates the phase matching frequencies across the various modes. As P_2 is tuned to shorter frequencies ($\Delta\omega$ increases), $\omega_{\text{BS},r}$ moves in the same direction, and an upshifted horizontal line can still be drawn to cross the two v_g^{-1} curves at the new average frequencies, as long as each v_g^{-1} curve is an exact (frequency-shifted) replica of the other. On the other hand, $\omega_{\text{BS},b}$, which also satisfies the energy conservation law, is shown to not satisfy phase matching in the example of Fig. 1 (bottom panel), since only an oblique line can be drawn to cross the two v_g^{-1} points at the corresponding average wavelengths. As P_2 is tuned to lower frequencies, $I_{\text{BS},b}$ moves further away from phase matching. It is worth noting that if the frequency of P_1 is tuned, the opposite discussion applies. This described phase matching mechanism can be utilized to efficiently suppress one idler, favoring a unidirectional FWM process. Indeed, one drawback of the BS-FWM is its bidirectionality, which might give rise to unwanted idler frequencies, thus reducing the conversion efficiency achievable at the desired (single) frequency [26]. This has been faced by the research community and, for example, in Refs. [26,27] the authors have proposed the use of cross-polarized pumps in birefringent fiber or integrated waveguides: by exploiting the different propagation properties exhibited by the two modes (orthogonal in polarization) they were able to effectively suppress one idler and favor the other one, opposite in direction. We note that similarities can be found between this scheme and the IM scheme we propose to use in this paper: both of them exploit the different propagation characteristics of two modes and in both cases the success of the scheme depends on the ability to keep the two modes involved decoupled during the propagation. To draw a comparison between the two schemes, we note that when the IM scheme is employed, the number of available modes that can be involved in the process is much larger than in the single-mode case [26] (limited to the two orthogonally polarized modes), thus granting additional flexibility in the design of the waveguide structure. Indeed, the scheme can be applied to any mode that is supported by the waveguide structure. As shown in Fig. 1 (bottom panel), when a higher-order mode (>1) is considered, the frequency distance between the pumps and idlers increases. As long as the v_g^{-1} curves of the considered modes satisfy the conditions stated above, the phase matching condition can still be achieved; therefore, the wavelength conversion can be realized for extremely large pump-to-signal detuning values. The described properties of the Bragg scattering IM-FWM make this scheme remarkably different from the single-mode case. As discussed, by using the scheme utilized in this work, broadband and unidirectional conversion can be obtained for very large pump-to-pump detuning values, with the original signal potentially placed at wavelength positions that are extremely distant from the pumps (for example, 50 nm when using TE00 and TE10 and >200 nm when using TE00 and TE30 modes) without the requirement to engineer the dispersion and the dispersion slope profiles of the waveguide (as for example discussed in Ref. [28]). This provides additional flexibility when designing the wavelength converter, in principle allowing for the realization of more complex devices.

3. SILICON-RICH SILICON NITRIDE WAVEGUIDE DESIGN

The waveguide was designed on the silicon-rich silicon nitride on oxide platform [22], and the geometry was a channel structure where a core material (silicon-rich silicon nitride) was encapsulated in a silicon oxide cladding. The device length was $L = 4$ cm. The propagation characteristics of the device were engineered by the control of two parameters: (i) the waveguide dimension and (ii) the core refractive index, which could be tuned by changing the silicon-rich silicon nitride material deposition conditions [22]. The cross-section of the designed waveguide is shown in Fig. 2 (inset). The silicon content, within the silicon nitride host matrix, was tuned to provide a material showing a refractive index of 2.54 at $\lambda = 1550$ nm. The waveguide dimensions were engineered to satisfy the phase matching condition between the fundamental and the first-order waveguide modes (TE00 and TE10, respectively). The results of a calculation of the corresponding group velocity curves are shown in Fig. 2. As shown, phase matching can be obtained between the TE00 and TE10 modes, e.g., at $\lambda_{\text{TE00}} = 1550$ nm and $\lambda_{\text{TE10}} = 1601$ nm, respectively. By considering these wavelengths and modes, we numerically simulated the bandwidth of BS IM-FWM efficiency [for both the $I_{\text{BS},r}$ and the $I_{\text{BS},r}$, efficiency defined as $\eta_{\text{IM-FWM}} = \frac{P_{\text{idler}}(L)}{P_S(L)}$, where $P_{\text{idler}}(L)$ and $P_{\text{signal}}(L)$ are the power of the idler $I_{\text{BS},r}$ or $I_{\text{BS},b}$ and the signal S measured at the end of the waveguide, respectively] as a function of the pump and signal wavelength detuning values. The waveguide modes and their dispersion were calculated using a finite-element method (Comsol Multiphysics where the refractive index of the silicon-rich silicon nitride was calculated from measured values of the bulk material employed in this work). The refractive index profile of the silica cladding was taken from the corresponding Sellmeier equation. The calculated modal effective index profiles and mode overlap factors were then used for nonlinear wave propagation simulations based on the multimode generalized nonlinear Schrödinger equation (MM-GNLSE) [8]. The MM-GNLSE was implemented in MATLAB using a symmetrized split-step Fourier method with automatic step-size

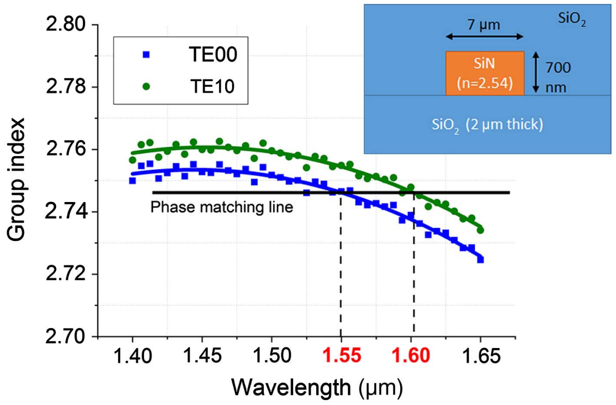

Fig. 2. Calculated group index for the first two waveguide modes (dots, simulations based on the measured refractive index of the silicon-rich silicon nitride material; line, polynomial fit). Inset: cross-section of the silicon-rich silicon nitride waveguide (not to scale).

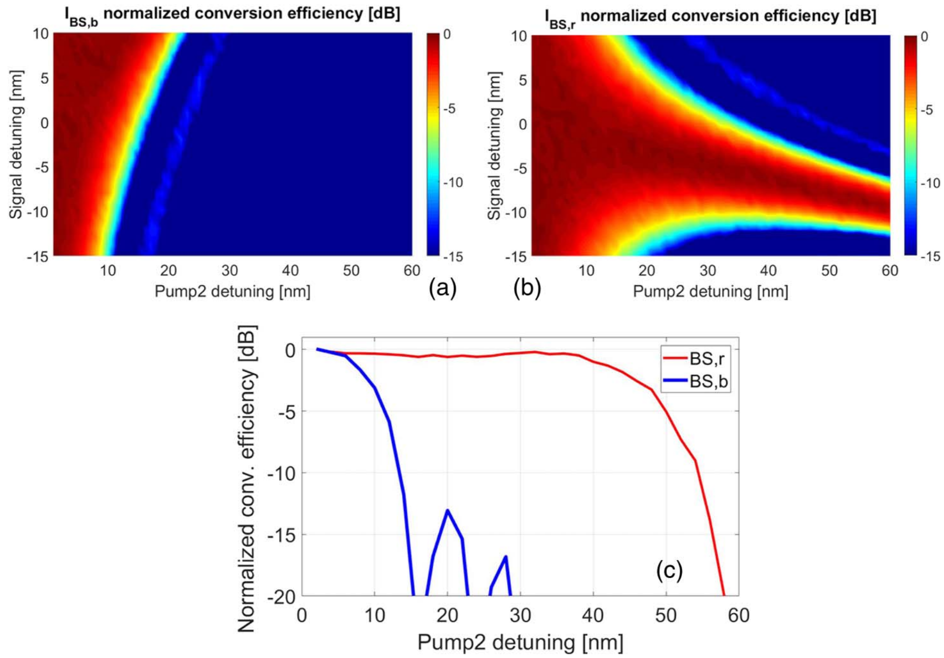

Fig. 3. Calculated BS-IM-FWM normalized efficiency for different pump-to-pump and pump-to-signal detuning values for (a) $I_{\mathrm{BS},b}$ and (b) $I_{\mathrm{BS},r}$. Numerical results showed that phase matching can be retained for high pump-to-pump detuning values. For instance, if pump 1 (P_1) is kept fixed and the second pump (P_2) is detuned to a longer wavelength, the phase matching bandwidth is more than 60 nm for the $I_{\mathrm{BS},r}$ idler (see right panel), while it is significantly shorter for the $I_{\mathrm{BS},b}$ idler (see left panel). It is worth noting that opposite results would be achieved if P_2 was kept constant, and P_1 moved to shorter wavelength values. (c) Numerical results for a specific value of signal detuning (-5 nm from the phase matched wavelength) for the BS, b (blue line) and BS, r (red line) idlers.

control of a 4th–5th-order Runge–Kutta solver. For each simulation (set of pump, signal, idler wavelengths), a frequency grid of 2^{15} points was defined to ensure that each relevant (CW) wave coincided with a single-frequency grid point. The nonlinear refractive index was set to $n_2 = 1.6 \times 10^{-18}\ \mathrm{m}^2/\mathrm{W}$ for the Kerr nonlinearity while Raman scattering was neglected [22]. In these simulations, the short-wavelength pump was kept fixed at 1550 nm, while $\Delta\omega$ was allowed to vary by modifying the wavelength of the second pump. In all cases, the pump power levels (total power) were kept at 20 dBm. The results are shown in Fig. 3 and reveal that it is possible to obtain a constant level of $I_{\mathrm{BS},r}$ conversion efficiency even for large P_2 detuning values (>50 nm). In contrast, the blueshifted idler $I_{\mathrm{BS},b}$ is not favored in this scenario, and it is only observed over a narrow range of pump-to-pump detuning. The figure also shows that for relatively small pump-to-pump detuning values (<10 nm), the conversion process to both $I_{\mathrm{BS},b}$ and $I_{\mathrm{BS},r}$ is rather insensitive to the signal wavelength, which can be tuned by over 25 nm around the phase matching wavelength ($\lambda_{\mathrm{TE10}} = 1601$ nm) with no significant degradation in conversion efficiency.

The efficiency level of the IM-FWM process is also determined by taking into account the spatial overlap of the interacting modes Q_{plmn}, where p, l, m, and n are the modes excited by the interacting waves. If the two first-order modes are considered (TE00 and TE10), Q is nonzero only in the following cases [29]:

- four waves in the TE00 mode,
- four waves in the TE10 mode,
- two waves in the TE00 mode and two waves in the TE10 mode,

where the top two configurations represent two cases of intramodal FWM (no interaction between different spatial modes is present). In the configuration considered here, two waves (pumps) were placed in the TE00 mode and two waves (signal and idler) in the TE10 mode. In this case Q_{0101} can be calculated as

$$Q_{0101} = \frac{\int |E_0|^2 |E_1|^2 \mathrm{d}x\mathrm{d}y}{\int |E_0|^2 \mathrm{d}x\mathrm{d}y \int |E_1|^2 \mathrm{d}x\mathrm{d}y}, \tag{4}$$

where E_0 and E_1 represent two generic mode fields of the corresponding waves. The calculated Q_{0101} for our designed waveguide [see Fig. 2 (inset)] was $0.21\ \mu\mathrm{m}^{-2}$, and the corresponding effective area $A_{\mathrm{eff}}(\mathrm{TE00}, \mathrm{TE10})$ was $4.652\ \mu\mathrm{m}^2$.

4. WAVEGUIDE FABRICATION

The silicon-rich silicon nitride layers were fabricated starting from a 150 mm diameter $\mathrm{SiO_2}$-on-Si substrate wafer. Nitride layers were deposited using a plasma-enhanced chemical vapor deposition (PECVD) tool (model OIPT SYS 100), by employing the following precursor gases: $\mathrm{SiH_4} = 3.6$ sccm (standard cubic centimeter per minute) and $\mathrm{N_2} = 980$ sccm at a chamber temperature of 350°C. The chamber pressure and RF power were set to 980 mTorr (1 Torr = 133.32 Pa) and 60 W, respectively. After deposition, waveguides were written using a waveguide layout designed to provide different test structures, including straight, spiral waveguides, and fiber-to-chip coupling devices. The mask layout was transferred to the wafers using E-beam patterning (positive electron beam resist ZEP 520A was used). After the development of photoresist, inductively coupled plasma (ICP) etching was performed to define the waveguide patterns on the light guiding layer. The remaining resist was removed by ashing in oxygen plasma. The protective, 1 μm thick, SiO_2 cladding layer was finally deposited by PECVD using a standard recipe for the deposition of stoichiometric SiO_2. Finally, the samples were cleaved to provide access to the butt-coupling devices. The coupling and propagation losses of the waveguide (for both the TE00 and TE10 modes) were assessed to be 2.9 dB and 0.95 dB/cm, respectively.

5. EXPERIMENTAL RESULTS

The experimental setup used to perform the BS IM-FWM experiments is shown in Fig. 4. Two C-band CW pump waves were combined at the input of an optical amplifier (OA) and coupled with a tunable L-band signal using a free space beamsplitter. The pumps were maintained in the fundamental (LP01-shaped) mode, while the signal was converted into the LP11-shaped mode using a mode-multiplexer (MMUX) based on a bulk optic phase plate (PP). The MMUX (red shaded area in Fig. 4) worked by shifting the phase of half of the beam front of the signal wave in the transverse plane by π. All the waves were linearly polarized and aligned with the TE polarization of the waveguide using polarization controllers and a polarization beam splitter (PBS). The optical beam was coupled to the waveguide through a 40× objective, by means of the end-fire coupling technique. The LP01-shaped mode excited the TE waveguide fundamental mode (TE00), while the LP11-shaped mode excited the TE10 waveguide mode (see corresponding inset images of Fig. 4 for their spatial mode distributions after propagation in the waveguide). Note that these mode images were obtained by inputting only one wave at a time through the sample. The beams at the output of the waveguide were coupled back to a single-mode fiber using a second 40× objective and a mode demultiplexer (MDMUX, blue-shaded area in Fig. 4). To demultiplex the two spatial modes (TE00 and TE10), a second bulk optic PP was placed before the output single-mode fiber. The MDMUX allowed extinction of either the TE00 or the TE10 optical mode, with a measured modal purity of, at least, 10 dB. Output optical spectra were recorded using an optical spectrum analyzer (OSA).

Our first set of measurements aimed to verify the pump-to-pump detuning bandwidth for both the $I_{BS,r}$ and $I_{BS,b}$ idlers. Following the results of our numerical simulations (Fig. 3), we initially placed the two pumps at wavelengths $\lambda_{P1} = 1550$ nm and $\lambda_{P2} = 1551$ nm, while the signal was placed at $\lambda_S = 1601.5$ nm. λ_{P2} was then gradually detuned to longer wavelengths, and the BS IM-FWM conversion efficiency was recorded. Figure 5 reports some typical spectra for a total pump power of 32 dBm. In Figs. 5(a) and 5(b), we show the spectra recorded for two different pump-to-pump detuning values (2 nm and 30 nm), as measured at the TE00 [Fig. 5(a)] and the TE10 [Fig. 5(b)] output ports. We also report results obtained when all waves were placed in the TE00 mode (i.e., no IM-FWM scheme), and the recorded spectra, for two different pump-to-pump detuning values (2 nm and 30 nm), are shown in Fig. 5(c). It is interesting to note that, when the pump-to-pump detuning is low, intraband FWM components are also generated (I_1 and I_2) that are the result of the degenerate FWM process among P_1 and P_2 (all placed in the TE00 mode).

It can be observed that the power level of the generated $I_{BS,r}$ remained constant, even when the P_2 detuning was about 30 nm [Fig. 5(b)]. This is in contrast to $I_{BS,b}$, which was no longer detectable when the P_2 detuning reached 30 nm. These results are summarized in Fig. 6(a) and confirm the numerical simulations of Fig. 3, demonstrating the broadband nature of the IM-FWM phase matching mechanism. It is worth noting that the intramodal FWM showed higher efficiency at very low pump-to-pump detuning values (2 dB higher than its IM-FWM counterpart). As discussed in the previous section, the efficiency of the FWM process also depends on the overlap integral among the four waves involved in the process [see Eq. (3)]. Since $Q_{0000} > Q_{0101}$, the intramodal FWM process resulted in higher efficiency for the same pump power levels when phase matching was satisfied. However, for P_2 detuning values >5 nm, phase matching was quickly lost in the intramodal case, making this process less efficient than its IM counterpart. A second set of measurements was conducted to characterize the IM-FWM signal detuning bandwidth. In this case, the two pumps were initially placed at $\lambda_{P1} = 1550$ nm and $\lambda_{P2} = 1551$ nm (total launched power in the waveguide 32 dBm), while the position of λ_S was varied between $\lambda_1 = 1580$ nm and $\lambda_2 = 1620$ nm. Using this wavelength configuration, we recorded the IM-FWM efficiency values for both the generated $I_{BS,r}$ and $I_{BS,b}$; the results are shown in Fig. 6(b) (red and blue squares, respectively). The results show no efficiency reduction, even for signal detuning values of ±20 nm (relative to the predicted phase matching wavelength of 1601 nm). We repeated the measurements for $I_{BS,r}$, with a pump-to-pump detuning of 30 nm ($\lambda_{P1} = 1550$ nm and $\lambda_{P2} = 1580$ nm); the results are shown in Fig. 6(b) (red/black squares). In this case, the phase matching condition was not retained across the full range of scanned wavelengths, and a 3-dB bandwidth of 20 nm was observed, centered around $\lambda = 1603$ nm. We note that the experimental results are in agreement with the numerical simulations.

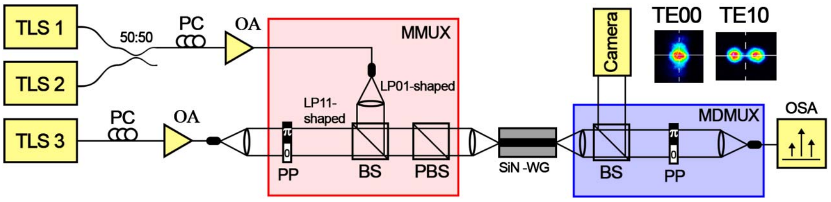

Fig. 4. Experimental set-up. TLS: tunable laser source. OA: optical amplifier. PC: polarization controller. BS: beam splitter. PBS: polarization beam splitter. PP: phase plate. SiN-WG: silicon-rich silicon nitride waveguide.

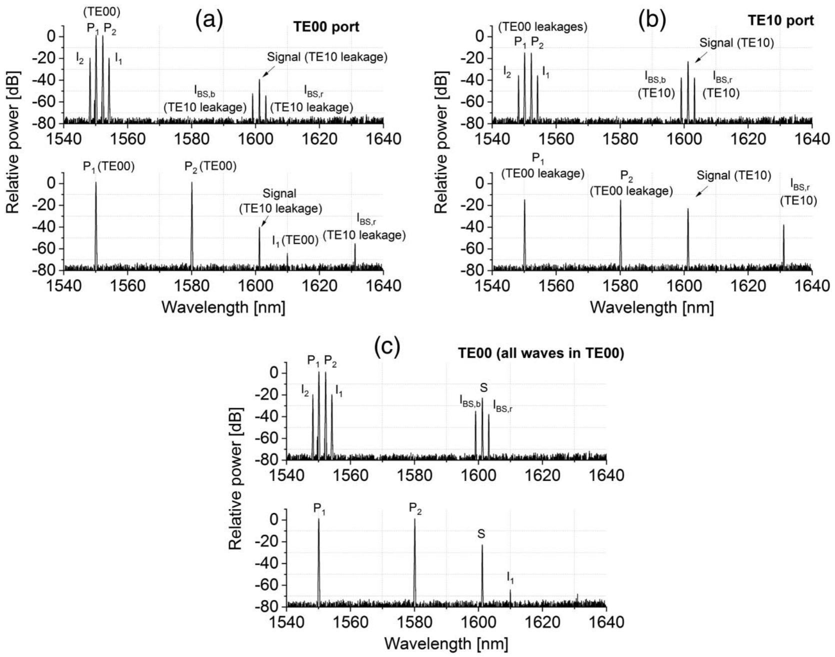

Fig. 5. Recorded spectra at (a) the TE00 port, when P_1 and P_2 were launched in the TE00 mode, while S was launched in the TE10 mode; (b) the TE10 port, when P_1 and P_2 were launched in the TE00 mode, while S was launched in the TE10 mode; and (c) the TE00 port, when all waves were launched in the TE00 mode (i.e., no intermodal FWM).

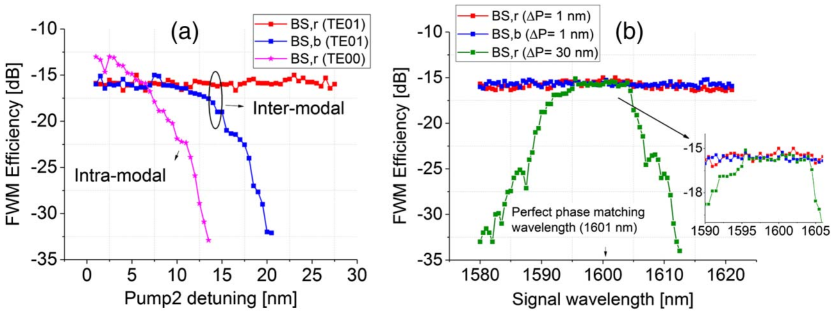

Fig. 6. (a) FWM efficiency measured for different pump-to-pump detuning values for the IM scheme (red and blue squares) and for the intra-modal scheme (magenta stars); (b) IM-FWM efficiency as a function of the signal wavelength (pump power 32 dBm) for $I_{\mathrm{BS},r}$ and $I_{\mathrm{BS},b}$ when the pump-to-pump detuning was 1 nm (red and blue squares, respectively) and for $I_{\mathrm{BS},r}$ when the pump-to-pump detuning was 30 nm (green squares). The inset shows a zoom-in of the plot in the region of perfect phase matching.

In particular, the numerical simulations predicted an IM-FWM bandwidth exceeding 50 nm [see Fig. 3(b)] when the TE00 and the TE10 modes are used and the $I_{\mathrm{BS},r}$ is considered. In these conditions, we measure a flat IM conversion efficiency across the whole available bandwidth (30 nm) limited only by our instrumentation. For this reason, we cannot fully verify the predictions made by the numerical analysis (which would require positioning the pump 2 wavelength beyond $\lambda_{P2} = 1580$ nm). Referring to the conversion bandwidth of $I_{\mathrm{BS},b}$ (blue curve in Fig. 6), we note that the measured 3-dB bandwidth (15.1 nm) is slightly broader than predicted by the numerical simulations (12 nm). We believe this discrepancy can be attributed to waveguide imperfections that might alter the dispersion profile of the obtained waveguide. The results presented in Fig. 6(b) are also in good agreement with the numerical simulations, thus confirming that the fabricated waveguides showed a very low dispersion value. This allowed the signal to be flexibly positioned at relatively distant wavelength values with respect to the perfect phase matching position ($\lambda_S = 1601$ nm), without compromising the IM-FWM conversion efficiency.

6. CONCLUSION

In this work, we have demonstrated the generation and conversion of signals in a silicon-rich silicon nitride waveguide, using a dual-pump FWM Bragg scattering scheme that employed two different spatial modes, TE00 and TE10. The silicon-rich silicon nitride material allowed us to operate the wavelength conversion device with high CW pump power levels (>30 dBm) with no sign of detrimental two-photon absorption and free carrier absorption effects. A maximum conversion efficiency of −15 dB was measured in this work, mainly limited by the waveguide propagation losses. We believe that additional material and fabrication developments could lead to a significant reduction in losses, thus allowing the use of longer waveguide sections and hence to obtain higher conversion efficiency values. Moreover, this demonstration shows the potential of the IM-FWM phase matching scheme, which allows frequency generation over multiple discrete bands, with pump-to-pump bandwidths exceeding 30 nm. The availability of integrated MMUX and MDMUX devices would allow the waveguide to operate with higher-order spatial modes (i.e., TE02 and TE03), potentially enabling wavelength conversion and generation in the MID-IR region, with negligible degradation in IM-FWM efficiency.

Funding. Engineering and Physical Sciences Research Council (EPSRC) (EP/L00044X/1).

Acknowledgment. This work was supported by the Engineering and Physical Sciences Research Council (EPSRC) through the project Silicon Photonics for Future Systems (SPFS). Data are openly available at the University of Southampton Repository: http://doi.org/10.5258/SOTON/D0425.

REFERENCES

1. G. P. Agrawal, *Nonlinear Fiber Optics*, 5th ed. (Academic, 2013).
2. M. A. Foster, A. C. Turner, J. E. Sharping, B. S. Schmidt, M. Lipson, and A. L. Gaeta, "Broad-band optical parametric gain on a silicon photonic chip," Nature **441**, 960–963 (2006).
3. S. Zlatanovic, J. Park, S. Moro, and J. Boggio, "Mid-infrared wavelength conversion in silicon waveguides using ultracompact telecom-band-derived pump source," Nat. Photonics **4**, 561–564 (2010).
4. F. Parmigiani, P. Horak, Y. Jung, L. Grüner-Nielsen, T. Geisler, P. Petropoulos, and D. J. Richardson, "All-optical mode and wavelength converter based on parametric processes in a three-mode fiber," Opt. Express **25**, 33602–33609 (2017).
5. J. Demas, G. Prabhakar, T. He, S. Ramachandran, and S. Ramachandran, "Broadband and wideband parametric gain via intermodal four-wave mixing in optical fiber," in *Conference on Lasers and Electro-Optics* (2017), paper SM3M.1.
6. R. Essiambre, M. A. Mestre, R. Ryf, A. H. Gnauck, R. W. Tkach, A. R. Chraplyvy, Y. Sun, X. Jiang, and R. Lingle, "Experimental investigation of inter-modal four-wave mixing in few-mode fibers," IEEE Photon. Technol. Lett. **25**, 539–542 (2013).
7. C. Lacava, M. A. Ettabib, G. Sharp, Y. Jung, P. Petropoulos, and D. J. Richardson, "Silicon photonics wavelength converter based on intermodal four wave mixing Bragg scattering," in *15th International Conference on Group IV Photonics (GFP)* (2018), pp. 99–100.
8. F. Poletti and P. Horak, "Description of ultrashort pulse propagation in multimode optical fibers," J. Opt. Soc. Am. B **25**, 1645–1654 (2008).
9. A. B. Kalifa, A. B. Salem, and R. Cherif, "Multimode supercontinuum generation in As_2S_3 chalcogenide photonic crystal fiber," in *Frontier in Optics* (2018), paper JTu2A.18.
10. Z. S. Ezhaveh, M. Eftekhar, J. A. Lopez, M. Kolsik, H. L. Aviles, F. Wise, D. Christodoulides, and R. A. Correa, "Blue-enhaced supercontinuum generation in a graded-index fluorine-doped multimode fiber," in *Optical Fiber Communication Conference* (2018), paper Th3D.2.
11. R. Dupiol, K. Krupa, A. Tonello, M. Fabert, D. Modotto, S. Wabnitz, G. Millot, and V. Couderc, "Interplay of Kerr and Raman beam cleaning with a multimode microstructure fiber," Opt. Lett. **43**, 587–590 (2018).
12. J. Demas, L. Rishøj, X. Liu, G. Prabhakar, and S. Ramachandran, "High-power, wavelength-tunable NIR all-fiber lasers via intermodal four-wave mixing," in *Conference on Lasers and Electro-Optics* (2017), paper JTh5A.8.
13. L. Rishøj, Y. Chen, P. Steinvurzel, K. Rottwitt, and S. Ramachandran, "High-energy fiber lasers at non-traditional colours, via intermodal nonlinearities," in *Conference on Lasers and Electro-Optics* (2012), paper CTu3M.6.
14. R. Guenard, K. Krupa, R. Dupiol, M. Fabert, A. Bendahmane, V. Kermene, A. Desfarges-Berthelemot, J. L. Auguste, A. Tonello, A. Barthélémy, G. Millot, S. Wabnitz, and V. Couderc, "Kerr self-cleaning of pulsed beam in an ytterbium doped multimode fiber," Opt. Express **25**, 4783–4792 (2017).
15. Y. Ding, J. Xu, H. Ou, and C. Peucheret, "Mode-selective wavelength conversion based on four-wave mixing in a multimode silicon waveguide," Opt. Express **22**, 127–135 (2014).
16. S. M. M. Friis, I. Begleris, Y. Jung, K. Rottwitt, P. Petropoulos, D. J. Richardson, P. Horak, and F. Parmigiani, "Inter-modal four-wave mixing study in a two-mode fiber," Opt. Express **24**, 30338–30349 (2016).
17. M. Guasoni, F. Parmigiani, and D. J. Richardson, "Novel fiber design for wideband conversion and amplification in multimode fibers," in *European Conference on Optical Communication* (2017), pp. 181–183.
18. O. F. Anjum, M. Guasoni, P. Horak, Y. Jung, P. Petropoulos, D. J. Richardson, and F. Parmigiani, "Polarization-insensitive four-wave-mixing-based wavelength conversion in few-mode optical fibers," J. Lightwave Technol. **36**, 3678–3683 (2018).
19. S. Signorini, M. Mancinelli, M. Bernard, M. Ghulinyan, G. Pucker, and L. Pavesi, "Broad wavelength generation and conversion with multi modal four wave mixing in silicon waveguides," in *Group IV Photonics* (2017), pp. 59–60.
20. R. Dupiol, A. Bendahmane, K. Krupa, A. Tonello, M. Fabert, B. Kibler, T. Sylvestre, A. Barthelemy, V. Couderc, S. Wabnitz, and G. Millot, "Far-detuned cascaded intermodal four-wave mixing in a multimode fiber," Opt. Lett. **42**, 1293–1296 (2017).
21. J. Yuan, Z. Kang, X. Zhang, X. Sang, B. Yan, F. Li, K. Wang, C. Yu, H. Y. Tam, and P. K. A. Wai, "Experimental demonstration of intermodal four-wave mixing by femtosecond pump pulses at 1550 nm," J. Lightwave Technol. **35**, 2385–2390 (2017).
22. C. Lacava, S. Stankovic, A. Khokhar, T. Bucio, F. Gardes, G. Reed, D. Richardson, and P. Petropoulos, "Si-rich silicon nitride for nonlinear signal processing applications," Sci. Rep. **7**, 22 (2017).
23. K. Uesaka, K. K.-Y. Wong, M. E. Marhic, and L. G. Kazovsky, "Wavelength exchange in a highly nonlinear dispersion-shifted fiber: theory and experiments," IEEE J. Sel. Top. Quantum Electron. **8**, 560–568 (2002).
24. A. C. Turner, C. Manolatou, B. S. Schmidt, M. Lipson, M. A. Foster, Y. Okawachi, and A. L. Gaeta, "Tailored anomalous group-velocity dispersion in silicon waveguides," Opt. Express **14**, 4357–4362 (2006).
25. F. Parmigiani, M. Guasoni, O. F. Anjum, P. Horak, Y. Jung, L. Gruner-Nielsen, P. Petropoulos, and D. J. Richardson, "Polarization insensitive wavelength conversion in a few mode fibre," in *European Conference on Optical Communication* (2017), paper W2F2.
26. J. B. Christensen, J. G. Koefoed, B. A. Bell, C. J. McKinstrie, and K. Rottwitt, "Shape-preserving and unidirectional frequency conversion using four-wave mixing Bragg scattering," Opt. Express **26**, 17145–17157 (2018).
27. B. Bell, C. Xiong, D. Marpaung, C. McKinstrie, and B. Eggleton, "Unidirectional wavelength conversion in silicon using four-wave mixing driven by cross-polarized pumps," Opt. Lett. **42**, 1668–1671 (2017).
28. D. Méchin, R. Provo, J. D. Harvey, and C. J. McKinstrie, "180-nm wavelength conversion based on Bragg scattering in an optical fiber," Opt. Express **14**, 8995–8999 (2006).
29. Y. Xiao, R.-J. Essiambre, M. Desgroseilliers, A. M. Tulino, R. Ryf, S. Mumtaz, and G. P. Agrawal, "Theory of intermodal four-wave mixing with random linear mode coupling in few-mode fibers," Opt. Express **22**, 32039–32059 (2014).